Mode-Locking in Semiconductor Fabry-Pérot Lasers

Julien Javaloyes and Salvador Balle

Abstract—We theoretically study the dynamics and the mode-locking properties of semiconductor Fabry–Pérot lasers with intracavity saturable absorber by using a travelling-wave model and a time-domain description of the optical response of the semiconductor materials. Our description enables us to incorporate important features as for instance the abrupt spectral variations of the absorption in the saturable absorber. We analyze the influence of several key parameters that affect the stability of the mode-locking regime and show that this modelling approach can be used, upon proper fitting of the material parameters, for optimization of the design of semiconductor mode-locked lasers.

Index Terms—Mode locked lasers, saturable absorber, semiconductor lasers, travelling-wave modelling.

I. INTRODUCTION

MODE-LOCKING (ML) of lasers is a subject of intense research both theoretically and experimentally. The theoretical challenge arises from the complex nonlinear dynamics involving the self-organization of many laser modes while the experimental motivation comes from the large number of applications of short pulse sources in medicine, metrology and telecommunications [1]. ML has led to the shortest and most intense optical pulses ever generated. Semiconductor mode-locked lasers have the added attraction of being compact, low cost and adaptable to many cavity geometries [2].

A multimode laser can be forced to operate in a mode-locked state either passively or actively. Active ML is achieved by modulating one control parameter of the laser at a frequency resonant with the separation between modes. A drawback of active ML is the requirement of a precise external modulation which can be unreachable at ultra-fast speeds. On the other hand, passive ML does not require any external modulation and it is the preferred approach for generating optical pulses at multi-gigahertz repetition rates [1]. Passive ML is commonly achieved by combining two elements, a laser amplifier which provides gain and a saturable absorber (SA) acting as a pulse shortening element. A window for amplification is opened around the pulse due to the faster recovery time of the absorption that can be either smaller or faster than the pulse width thereby defining the

two so-called regimes of slow [3] and fast [4] SA. Often, the two methods can be combined effectively (hybrid ML) to reduce pulse jitter, as for instance in [5], where timing jitter as low as 570 fs is obtained by direct modulation of the SA section. Notice however that alternative methods exist, e.g., nonlinear polarization rotation [6], Kerr lens mode locking [7] as well as crossed-polarization gain modulation [8] or ultrafast Stark effect modulation [9].

Despite the effort that has been dedicated to it, modeling of ML lasers continues to present a challenge. Haus' master equation is a widely used approach to study passive ML in the time domain. Because analytical predictions on the pulse properties can be assessed, these pulse iterative models have provided some very useful insights into the ML problem. However, these approaches when applied to a particular design provide only some very qualitative predictions due to the many simplifying hypothesis involved. For instance, the assumption of weak gain and saturation is difficult to justify in semiconductor media. This hypothesis was however lifted by the more refined model presented in [10]. Still, the work presented in [10] assumes a lumped element approach, where gain, loss and linear spectral filtering happen in different sections of the device, as well as an ideal unidirectional ring configuration. While the former hypothesis of lumping gain and a linear filtering element could be valid when a strong filter is present within the cavity, e.g., a distributed Bragg reflector, it is however usually the gain medium itself that provides the spectral filtering of the pulse. This spectral transformation is furthermore nonlinear [11], [12]. In addition, the saturable loss section also provides a strongly asymmetric and non linear filtering, a point that is usually overlooked. The latter hypothesis of unidirectional emission strongly restricts the scope of the possible cavity geometries thereby excluding the common case of a Fabry–Pérot cavity.

On the other hand, approaches based on a finite difference time domain description of the electromagnetic field [13] and the many body semiconductor Bloch equations description of the active medium [14] allow to satisfactorily describe ultrafast dynamics. However, they require an enormous computational power which impedes parametric studies thereby hindering a comprehensive understanding of the ML scenario: even if ML is by definition a fast phenomenon, pulses being of the order of the picoseconds, the transient time needed to reach a stable emission regime can be as long as several tens of nanoseconds, representing thousands of cycles; in addition, assessing timing jitter or pulse fluctuations requires computing long time series.

To circumvent the limitations of these models and shed some light onto the ML scenario, another approach consists of describing the dynamics by spatially resolving the propagation of the electromagnetic waves under the slowly varying approximation, thereby going from resolutions below the wavelength to resolutions of a few tens of the wavelength. Such an ap-

J. Javaloyes is with the Department of Electronics and Electrical Engineering, University of Glasgow, G12 8LT Glasgow, Scotland, U.K. (e-mail: julien.javaloyes@elec.gla.ac.uk).

S. Balle is with the Institut Mediterrani d'Estudis Avançcats (IMEDEA), Consejo Superior de Investigaciones Científicas-Universitat de les Illes Balears, E-07071 Esporles, Spain (e-mail: salvador@imedea.uib-csic.es).

proach, based on a travelling-wave model (TWM) of the device, allows to directly incorporate the inhomogeneous spatial distributions of the optical field and material variables, the so-called spatial-hole burning effects. Moreover, this approach allows to study different designs irrespective of the geometry, which enters the description of the system via the boundary conditions to be satisfied by the optical field.

Although the TWM can be used with a frequency-independent gain spectrum [15], more quantitative studies have to include this feature, which poses the main difficulty faced in TWMs: to correctly describe the interaction of the optical field with the active material in time domain. A pioneering work incorporating frequency-dependent gain in a TWM dates back to the late 1960s [16] and was successfully used in, e.g., [17]. Still, these works assume the presence of a two-level active medium, for which the optical response in time domain is well known [18]. This is generally not the case of semiconductor materials, where the presence of energy bands induces a large inhomogeneous broadening [19] that profoundly affects the dynamics in semiconductor lasers. This has stimulated the search of approximate descriptions of the optical response of semiconductor media. In [20] the optical response, determined from the semiconductor Bloch equations, was fitted to the sum of several lorentzians, each of them allowing for a two-level like description. Other approaches [21], [22] have also developed two-level like approximations to the optical response of bulk semiconductor active media. Finally, analytical expressions for the optical response of quantum-well active media in simplified cases have been developed in [23] and [24]. These latter results, given only in the frequency domain, have been used in [25] by transforming them into a rational fraction by using a Padé approximation. While good for narrow band spectra, the results based on the rational fit presented in [25] are expected to be less accurate when a SA is present in the device. The first reason being simply that the SA induces broad band multimode dynamics; the second reason is that the spectral shape of the band-edge of the SA semiconductor material, which presents a sharp transition from transparent to absorptive behavior, is expected to be poorly described by any kind of fit based on polynomials or rational functions.

More recently, the analytical results of [24] have been transformed exactly into a time domain description [26] capable of dealing even with the sharp band-edge of SAs. This improved model allows us to study important physical effects that were beyond the reach of the model presented in [25] as for instance the strong influence of the relative position between the gain peak and the SA band-edge on the pulses [27]. This effect is particularly important in materials like AlGaInAs since their band-edge is extremely sharp (10–15 nm).

In this manuscript, we use the method presented in [26] to analyze the simple, yet poorly understood, configuration of a Fabry–Pérot laser with one section of SA at one end. Although commonly encountered in ML lasers, this configuration can hardly be studied by pulse iterative models. We discuss the dynamics of this specific system, focusing on the key parameters affecting the mode-locked regimes: length and recovery time of the SA section, gain bandwidth and relative position of the

band-edge of the SA with respect to the gain peak. We postpone for future studies the statistics of the pulse train.

This paper is organized as follows. In Section II, we recall the basis of our TWM and the implementation of the time domain polarization by a convolution presented in [26]. Section III discusses the parametric dependencies of the ML dynamics. Finally, we draw some conclusions in Section IV.

II. MODEL

Our theoretical framework is a TWM for the slowly-varying amplitudes of the forward and backward waves [18], $E_\pm$, which evolve in space and time according to

$$(\partial_t \pm \partial_z)E_\pm(z,t) = i\Gamma P_\pm(z,t) - \alpha_i E_\pm(z,t) \qquad (1)$$

where α_i are the internal losses of the system, Γ is the optical confinement factor, and for numerical purposes we have scaled time and space to the cavity transit time and to the optical length of the cavity, respectively. A typical 1.17 mm long device would have a transit time $\tau_c \sim 12.5$ ps.

In (1), the source for $E_\pm$ are the projections of the total polarization of the active material onto the forward and backward propagation directions, $P_\pm$, which are obtained by a coarse graining procedure by averaging the polarization over a few wavelengths. In addition, appropriate boundary conditions for the field amplitudes have to be provided for describing the geometry of the device. In our case, we shall consider a Fabry–Pérot cavity divided in two sections. The first one, from $z = 0$ to $z = 1 - l$ is electrically pumped and corresponds to the amplifier section; the second one, from $z = 1 - l$ to $z = 1$, is reverse biased and corresponds to a SA section of relative length l. We consider that there is no reflectivity at the amplifier-SA interface, and that the cavity is defined by simple cleaved facets.

Within each section, the link between the polarization and field amplitudes is given by [26]

$$P_\pm(z,t) = \int_0^\infty \tilde{\chi}[s, N_0(z,u)] E_\pm(z,u)ds$$
$$+ \int_0^\infty N_{\pm 2}(z,u)\frac{\partial \tilde{\chi}}{\partial N}[s, N_0(z,u)] E_\mp(z,u)ds \quad (2)$$

where $u = t - s$ and $\tilde{\chi}(s,N)$ is the Fourier transform of the frequency-dependent susceptibility of the active material. In addition, $N_0(z,t)$ is the quasi-homogeneous component of the spatially dependent, time evolving carrier density, while $N_{+2}(z,t) = N_{-2}^\star(z,t)$ is the complex amplitude of the carrier density grating at half the wavelength that develops due to the presence of the two counter-propagating waves. In deriving (2), we assumed that the grating in the carrier density is small due to carrier diffusion [25]. Using the analytical susceptibility developed in [23], [24], we have that [26]

$$\frac{\tilde{\chi}(s,N)}{\chi_0} = e^{-(\gamma_\perp + i\Omega)s}\frac{2e^{-i\frac{N}{Nt}\gamma_\perp s} - e^{-ib\gamma_\perp s} - 1}{s}\Theta(s) \quad (3)$$

where $\Theta(s)$ is the Heaviside function. Moreover, $\gamma_\perp$ is the polarization dephasing rate, N_t is the transparency carrier density, Ω the frequency corresponding to the bandgap, b the normalized energy span of the semiconductor bands and χ_0 the material's susceptibility constant (see [24] for details). Note that this response function is causal and well behaved at $s = 0$. The decaying exponential represents the memory time of the active medium, which is proportional to $\gamma_\perp^{-1}$ as intuition dictates.

We note that a typical polarization relaxation time of 125 fs corresponds in our scaled units to $\tilde{\gamma}_\perp \sim 100$. In addition, the energy span of a semiconductor typically gives $b \in [10^2 \ldots 10^3]$ [24]. It is however possible to choose a much lower value for the top of the band without any noticeable deformation of the gain and of the index spectra in the frequency range where the dynamics occurs [26], which very much simplifies the numerical implementation. In the following we use $b = 10$, which corresponds to an energy span $\Delta\nu = b\gamma_\perp/(2\pi) = 16$ THz, i.e., much larger than the optical width considered.

It is worth remarking that both the amplifier and the SA sections will be described with exactly the same functional form for the optical response, although with different parameter values. The reason is that both sections, even if having the same nominal composition, work in very different conditions for the carrier density. The polarization relaxation is typically mediated by two sources, phonon assisted and carrier induced relaxation. While the former one does not depend on the carrier density but mainly upon the quantity of phonons available, the second one is an increasing function of the carrier density. Since the gain and absorber sections operate in very different regimes where the carrier density is respectively large and small, the relaxation time in the SA must be longer, hereby determining that the values of χ_0 are different in the two sections. We will denote χ_g and χ_s their values in the gain and SA sections. In addition, we allow the band-edge of the SA section Ω_s to be shifted in frequency with respect to the one of gain section, thereby including in a phenomenological way the quantum confined stark effect. We choose our reference frame to be the band-edge of the gain section, therefore $\Omega_g = 0$.

Within the gain section, the carrier density is determined by

$$\partial_t N_0(z,t) = J - R(N_0) - i\left(P_+ E_+^\star + P_- E_-^\star - c.c.\right) \quad (4)$$

$$\partial_t N_{\pm 2}(z,t) = -\left(R'(N_0) + 4\mathcal{D}q_0^2\right)N_{\pm 2}$$
$$- i\left(P_\pm E_\mp^\star - E_\pm P_\mp^\star\right) \quad (5)$$

where J is the current density injected per unit time (normalized to the electron charge) into the section and $q_0 = (2\pi n_g)/\lambda$ is the optical carrier wavevector. The recombination term is assumed to be of the form

$$R(N) = AN + BN^2 + CN^3 \quad (6)$$

where A, B, and C the non radiative, bi-molecular and Auger recombination coefficients, respectively, and the ambipolar diffusion coefficient is $\mathcal{D}$.

Within the SA section, there is no current injection (hence $J = 0$) but the optically generated carriers are swept out at a

rate that depends on the reverse voltage applied to the SA section. In addition, impurities and defects—created e. g. by proton bombardment—can largely increase the non-radiative recombination rate in this section. As a result, the evolution of the carrier density in the SA section is given by formally the same equations as those in the gain section, with

$$J = B = C = 0 \quad (7)$$
$$A = \tau_s^{-1}. \quad (8)$$

The method used to numerically integrate the model is detailed in [26] and [28]. For numerical purposes it is convenient to scale the carrier densities within each section to the corresponding transparency carrier density, N_g in the gain section and N_s in the SA section. The fields and polarizations are then accordingly scaled. The field is spatially discretized on a mesh of M samples, hence the temporal discretization, fixed by the Courant–Friedrichs–Lewy condition is $h = 1/M$ (the speed of light and the length of the cavity are unity in our notations). This means that our signal is sampled and that the convolution has to be computed from a discretized signal. The highest order of integration achievable in this case is second order accurate, consistent with our integration algorithm for the partial differential equations. For a given second order accuracy, several variations for the integral can be used and we choose the trapezoidal rule, which besides being the simplest also happens to be the best (see [26] for more details). In addition, we simulate spontaneous emission noise by adding after each step a stochastic term to the polarization at each point in space and in each direction of variance β. We assume for the sake of simplicity that β is both frequency and carrier density independent. The noise was generated by the Box–Muller method and a Mersenne twister [29].

III. RESULTS

We consider unless otherwise specified the device parameters listed in Table I. The fundamental repetition rate of our ML device is 40 GHz. We have considered that the intraband relaxation time in the SA is double of that in the gain section and consequently $\chi_s = 2\chi_g$. This represents closely the case of Al quaternary materials as presented for instance in [30].

We summarize in Fig. 1 the various frequency scales present in the problem by representing the imaginary part of the susceptibility in the amplifier and SA sections for different values of the carrier density. The chosen values are smaller in the SA section since it is usually operating below transparency, i.e., $N/N_s \leq 1$. The gain and absorption of the active medium in the two sections have different references band-edge frequencies, i.e., Ω_g and Ω_s. Notice also that the SA band-edge is sharper since we have chosen $\gamma_g = 2\gamma_s$.

In this configuration and for the parameters of Table I the lasing threshold of the pure Fabry–Pérot laser is achieved when the carrier density in the gain section is around $N = 2N_g$. Therefore the effective FWHM of the gain spectrum estimated from Fig. 1(a) is 5 THz, i.e., 40 nm around the lasing wavelength of 1550 nm. With the parameters of Table I, this corresponds to a normalized current value of $J = 30$.

| Symbol	Value	Units	Meaning
λ_0	1.55	μm	Emission wavelength
n	3.6	-	Effective index
Γ	5%	-	Optical confinement factor
r	0.55	-	Facet reflectivity
τ_c	12.5	ps	Cavity transit time
α_i	15	cm^{-1}	Internal losses
Gain section			
Ω_g	0	GHz	Band-Edge Frequency
$2\chi_g$	2140	cm^{-1}	Gain factor
b	10	-	Empty band contribution
γ_g	8×10^{12}	s^{-1}	Polarization decay rate
N_g	1×10^{18}	cm^{-3}	Carrier Density at transparency
$\mathcal{D}$	16	$cm^2 s^{-1}$	Ambipolar diffusion coefficient
A	1×10^8	s^{-1}	Non radiative recombination
B	7×10^{-10}	$cm^3 s^{-1}$	Spontaneous recombination
C	1×10^{-29}	$cm^6 s^{-1}$	Auger recombination
SA section			
Ω_s	760	GHz	Band-Edge Frequency
$2\chi_s$	4280	cm^{-1}	Gain factor
b	10	-	Empty band contribution
γ_s	4×10^{12}	s^{-1}	Polarization decay rate
N_s	5×10^{17}	cm^{-3}	Carrier Density at transparency
τ_s	10	ps	SA recovery time
l	5%	-	SA relative length
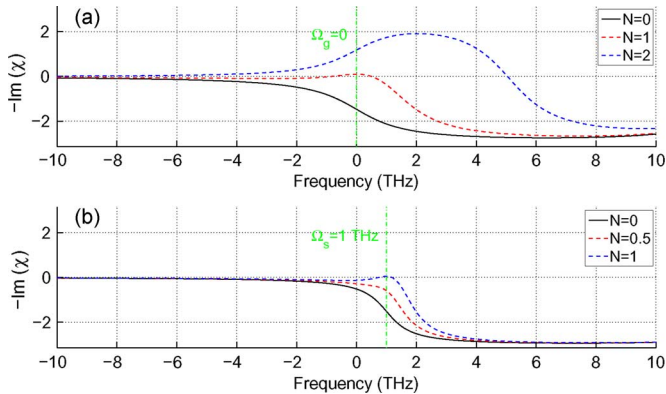
Fig. 1. Gain and absorption in the gain and the SA sections for different values of the carrier density normalized to transparency within each section.

A. Methods

The results presented next have been obtained with a spatial discretization of $M = 400$ points, while the length of the simulations is $10^4 M$ steps which corresponds to 10^4 single trips in the cavity, i.e., 125 ns. Preliminary studies indicate that this time is usually suitable for having a good description of the asymptotic dynamics: the typical transients usually do not last longer than 30 ns, although some critical slowing down can not be totally ruled out. We keep 10% of the final time trace to perform the data processing. A typical 125 ns simulation run is achieved in 15 min on a reasonably modern PC @ 2.6 GHz. Albeit beyond the scope of this manuscript, where we examine the parameters influence on the ML regimes, the method is practical for computing long time series and assess the statistics of the pulse train.

We obtained several bifurcation diagrams as a function of some key parameters in order to assess the operating range and the ML quality and stability. We used the typical method of numerical continuation: the final solution found for one value of the control parameter is used as an initial condition for the next, slightly different, value of the control parameter. An unique sweep of the control parameter, e.g., ramping up or down, would fail to detect possible bistable behavior. However, an unique scan usually gives some hint of a possible bistable behavior, like, e.g., a sharp transition in a bifurcation diagram. During this study, we did not find any of such hints and all the parameter sweeps are made only ramping up or down the control parameter if not otherwise stated.

The typical sequence of bifurcations found upon increasing of the bias current is: steady emission, weak multimode dynamics, stable ML, a bubble of self-pulsation if the SA modulation is sufficiently strong and finally a partial degradation of the pulse train for high drive current (ten times threshold). If not otherwise stated the value of the bias current corresponds to five times the threshold current.

We represented in the bifurcation diagrams of Figs. 3, 5, 7, and 9: a) the average, minimal, and maximal values of the field intensity at the right output; b) the carrier density in the middle of the cavity, i.e., within the gain section; and c) the carrier density in the SA at the right output, i.e., in the SA section, respectively. Average, maximal and minimal values are depicted in blue, red, and green, respectively. One should note that in panels a) the average value of the intensity was multiplied by 25, i.e., the round trip. This is important not only for clarity but also means that when the maximal intensity, i.e., the peak power, is of the same order as the steady intensity multiplied by the round-trip, one is dealing with pulses having a duty cycle of 1/25, i.e., a width of the order of 1 ps.

Panels d)–f) represent the average frequency of the optical spectrum, measured from the band-gap reference, the full width at half maximum (FWHM) of the *field* auto-correlation and the FWHM of the optical spectrum, respectively. The average frequency as well as the spectral FWHM were assessed by a Gaussian fit of the optical spectrum.

In the figures containing time traces, we represent the field intensity at the right facet, the maxima and minima, in blue, red and green respectively, while the right panel are simply a zoom on the pulse detail where, in order to ease the comparison, the pulses are normalized to their peak power.

B. Influence of the Saturable Absorber Length

We study in this section how the SA length affect the dynamics. Physical intuition indicates that a too short SA section would not induce a sufficient non linearity to sustain pulsed behavior. However, a too long section introduces too much losses in the device rendering its efficiency marginal. In between this two extreme cases, a large variety of regimes can be found in agreement with studies from other groups, see for instance [15]. Notice that due to the discrete nature of our spatial discretization, the minimal variation of the SA length l is $1/M = 0.25\%$. We scan l from $l = 0\%$ (simple Fabry–Pérot device) up to $l = 7.5\%$ which explain the relatively coarse nature of the diagrams presented in this section.

As the length of the SA is scanned, the following different behaviors are observed.
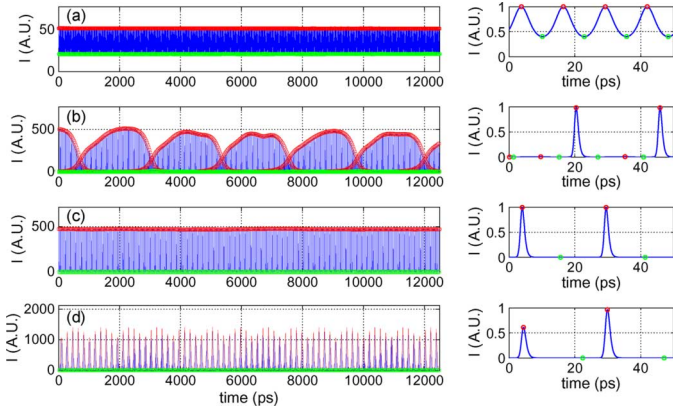
Fig. 2. Long time behavior of the time traces of the field intensity (left) and details of the pulse shape (right). The panels a)–d) correspond to $l = 1.5\%$, $l = 3\%$, $l = 3.75\%$, and $l = 6.5\%$, respectively.

1) For l ranging from 0% up to 1.25%, only weak multi-mode can be seen and the optical spectrum is essentially monomode.

2) For l between 1.5% and 2%, a transition to stable shallow Harmonic ML is found as can be seen in Fig. 2(a) obtained with 1.5%. The FWHM of the auto-correlation is not defined in this almost linear regime since the modulation is less than 50%.

3) For l ranging from 2% to 3% unstable ML appears, with substantial modulation of the pulse amplitudes which is accompanied by a considerable jitter as can be seen in the pulse train in Fig. 2(b), obtained with $l = 3\%$.

4) For l ranging from 3% to 5% stable ML exists with very low noise triggered jitter, see Fig. 2(c) with $l = 3.75\%$.

5) For l ranging from 5.25% up to 7.5% the device enters a Q-switch instability regime (QSI), see Fig. 2(d) obtained with $l = 6.5\%$.

A more comprehensive picture of the effect of the length of the SA section is provided by the bifurcation diagram shown in Fig. 3. When l is increased, the average intensity decreases since a higher absorber length corresponds to higher linear losses at threshold. Therefore the threshold current density and slope efficiency are respectively increased and decreased. This explain while the average intensity is a decreasing function of l while the carrier density is a increasing function of l. The SA average density decreases since, the longer the section, the more difficult it is to bleach the carriers at the right-most facet of the absorber. The shorter auto-correlation and the broader spectra are obtained around 3%, although in a weakly stable regime, simply because too short an absorber is not sufficient to trigger ML, and too long an absorber increases losses and in turn decreases the power available to modulate the absorber. In this respect, the statement that shortening the absorber shorten the pulse width, albeit true, is valid only when one is comparing the same current density, as it is the case in Fig. 3. One can also observe that the average frequency is red shifting when the saturable absorber length is increased. The longer the section, the bigger the penalty to operate in the blue when the absorption is large. The laser therefore adapts its frequency by shifting from the gain peak to the red in order to compensate for the quantity of absorption.
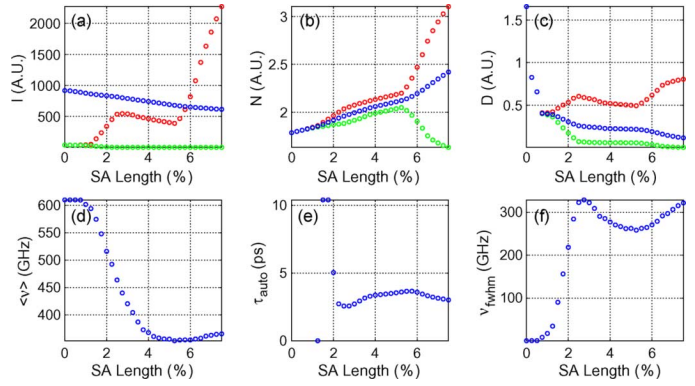

Fig. 3. Bifurcation diagram as a function of the SA Length, minima, maxima, and average values are depicted in green, red, and blue, respectively (see text for details).

C. Influence of the SA Recovery Time

Another parameter that strongly affects the pulse train quality as well as its stability is the recovery time of the SA. The increase of the SA recovery rate is usually obtained by increasing the reverse Voltage applied to the SA section. How should note however that this increase is usually accompanied by a red shift of the SA band-edge due to the Quantum confined Start effect. However, in order to be able to distinguish between the influence of the SA recovery time and of the SA Stark effect, we are only varying one control parameter in this section. The influence of the relative detuning between the gain and the SA section is deferred to Section III-E, and in this section we study only the influence of the recovery time for a fixed SA length $l = 5\%$.

The different behaviors obtained as the recovery time of the SA is reduced are presented in Fig. 4. The following can be observed.

1) For τ_s ranging from 50 down to 45 ps (not shown in Fig. 4), the laser is essentially monomode.

2) For τ_s ranging from 45 down to 26 ps, a weak multimode regime arises and steadily broadens as can be seen in Fig. 4 panels d) and c) obtained with a recovery time $\tau_s = 40$ and $\tau_s = 26$ ps, respectively.

3) For τ_s ranging from 25 down to 5 ps, a broad region of stable ML with typical auto-correlation FWHM of 3 ps exists, see for instance Fig. 4 panel b) obtained with $\tau_s = 25$ ps.

4) For τ_s ranging from 5 down to 1 ps, a sudden decrease of the auto correlation FWHM as well as a sudden increase of the spectral width indicates an improvement in the sharpness of the pulses train as can be seen Fig. 4 panel a) obtained with $\tau_s = 1$ ps.

The global picture of the effects of the recovery time of the SA can be found on the bifurcation diagrams plotted in Fig. 5.

One can clearly observe a qualitative change when $\tau_s \sim \tau_c$. For $\tau_s > \tau_c$, the emission frequency is substantially detuned to the blue, while for $\tau_s < \tau_c$ the detuning is substantially reduced. The reason is that, for long recovery times of the SA, the absorption at high frequencies is bleached more efficiently hence the system tends to operate close to the gain peak of the amplifier section; instead, for short recovery times the laser operates closer to the transparency frequency of the SA, where absorption can be bleached more easily.
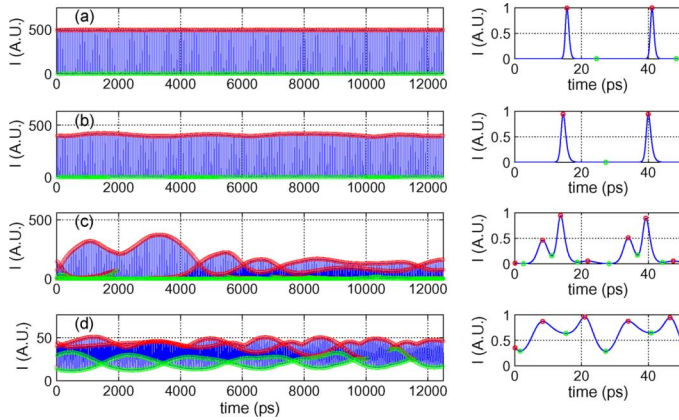
Fig. 4.   Long time behavior of the time traces of the field intensity (left) and details of the pulse shape (right). The panels a)–d) correspond to $\tau_{sa} = 1$, $\tau_{sa} = 25$, $\tau_{sa} = 26$, and $\tau_{sa} = 40$ ps, respectively.

In addition, a clear trend is also found on the auto-correlation diagram (see panel e): the pulse width does not depend much on the recovery time as long as it is longer than the pulse width and faster than the round trip repetition frequency, i.e., $5\,\text{ps} \lesssim \tau_s \lesssim 25\,\text{ps}$. This regime corresponds to the slow absorber regime [4], when the absorber tailors only the leading edge of the pulse. When τ_s is comparable with the pulse width, then some tailoring the trailing edge of the pulse takes place [3] which explains the decrease of the pulse width in this range. For the quite unrealistic values $\tau_s < 0.5$ ps, the SA becomes impossible to modulate efficiently, meaning that the stimulated term cannot dominate anymore the linear recovery time, even during the fast stage corresponding to the pulse induced depletion of the absorption. As a consequence, we did not find any ML, for this parameter set.

One also observes that the average intensity and the SA carrier density increase with the recovery time, while the average carrier density in the amplifier section decreases. Again, the reason is that for long recovery times of the SA, the carrier density in the SA section is higher hence leading to reduced absorption losses. The bleached absorption reduces the carrier density in the amplifier section required to equate gain and loss, and increases the output intensity.

The change of behavior is due to the fact that when τ_s reaches the value of the round-trip time τ_c, the SA has time enough to recover its full absorption between pulses. A word of caution is however needed: the occurrence of this transition almost exactly at $\tau_s = \tau_c$ is merely a coincidence of our parameter set, the transition has only to be expected *around* $\tau_{sa} = \tau_c$. However, it is clear that the condition $\tau_s < \tau_c$ is the most favorable for having a stable fundamental mode-lock regime in Fabry–Pérot lasers.

D. Influence of the Intraband Relaxation Time

The previous study indicates that the recovery time is clearly not the only mechanism governing the pulse width and stability. The pulse width should also be influenced by the number of modes capable of entering the ML state, which is expected to depend on the width of the gain spectrum. In order to assess the dominant mechanism governing the pulse width, we fix the SA length and recovery time to $l = 5\%$ and $\tau_s = 10$ ps, respectively
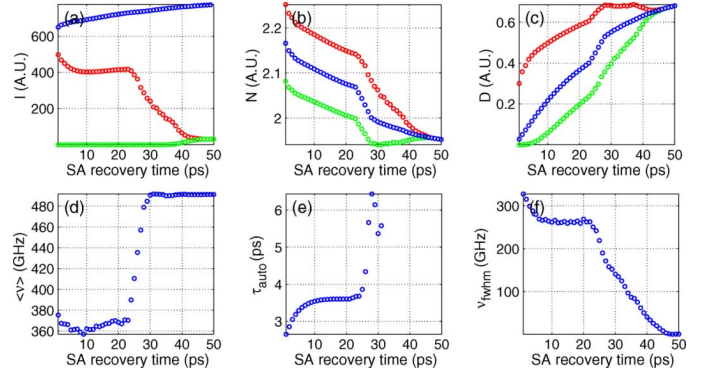

Fig. 5.   Bifurcation diagram as a function of the SA recovery time, minima, maxima and average values are depicted in green, red, and blue, respectively (see text for details).

and we vary the intraband time while the other fixed parameters are detailed in Table I. Note that, in order to compare with the previous results, we consider always that the dephasing time in the amplifier section is half that of the SA section, so we are simultaneously varying γ_g and γ_s.

Although the tunability the intraband relaxation time is not immediately clear from an experimental point of view, one should note that devices with higher thresholds operate with higher current density. This has a double effect: on one hand, the gain bandwidth is a strongly dependent function of the carrier density, on the other, the dephasing rate due to carrier-carrier collisions increases. Hence, tuning the intraband time leads to basically stretch or compress the susceptibility of the semiconductor in the frequency domain thereby mimicking devices operating with higher threshold current density.

With the chosen configuration, stable ML is found for all the values of γ_g considered, whose characteristics we present for the sake of completeness in Fig. 6(a)–(d), obtained with $\gamma_\perp / 10^{12}$ equal to 1, 5, 9, and 13, respectively.

The bifurcation diagram in Fig. 7 evidences the clear linear dependence of the auto-correlation FWHM as a function of the intraband recovery time $\gamma_\perp^{-1}$, while the FWHM of the optical spectra is directly proportional to the inverse of the intraband time, $\gamma_\perp$. As the pulse compresses, the peak power increases in Fig. 7(a) and the SA is more efficiently modulated in Fig. 7(c).

This study allows us to conclude that the breadth of the gain curve is the dominant quantity limiting pulsewidth. Notice that in our approach the susceptibility linking field and polarization is complex. As such the gain curvature is accompanied by dispersive effects. The imaginary part of the second derivative of χ in the frequency domain determines the modal threshold difference while its real part is the so-called group velocity dispersion (GVD). In our approach, one can not distinguish whether the modal gain difference or the fact that modes are not equidistributed in frequency domains is what limits pulsewidth. However, our analysis suggests that an important control on the pulse characteristics could be expected by the inclusion of a grating. Depending on the relative spectral width of the grating, one can expect either a broadening of the pulses whenever the grating spectral FWHM is smaller than that of the semiconductor gain curve, usually meaning pulses closer to the transform limit. Opposingly, when the grating possesses a comparable FWHM to the one of the active material, one can obtain a shortening of the
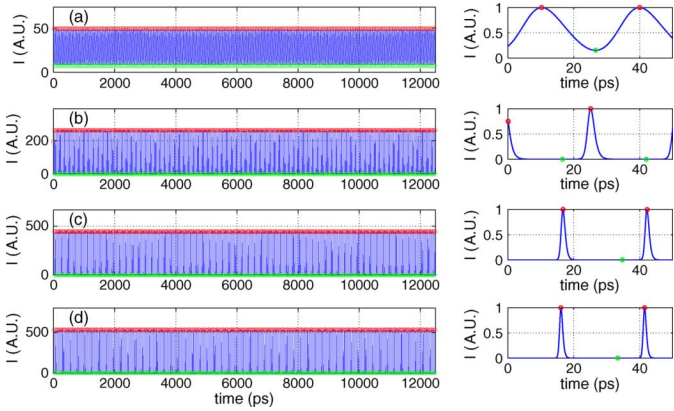
Fig. 6. Long time behavior of the time traces of the field intensity (left) and details of the pulse shape (right). The panels a)–d) correspond to $\gamma_\perp / 10^{12}$ equal to 1, 5, 9, and 13, respectively.
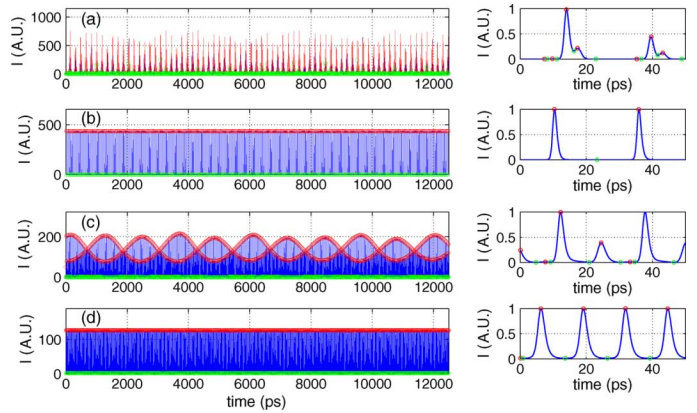

Fig. 8. Long time behavior of the time traces of the field intensity (left) and details of the pulse shape (right). The panels a)–d) correspond to Ω_{sa} equal to 0.6, 1.3, 1.8, and 2.1 THz, respectively.
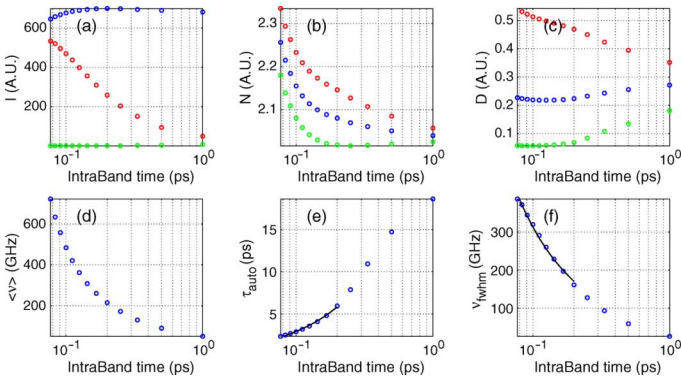

Fig. 7. Bifurcation diagram as a function of the intraband polarization dephasing time, minima, maxima and average values are depicted in green, red and blue, respectively (see text for details). The black lines in panel e) and f) correspond to the best linear fits as a function of $\gamma_\perp^{-1}$ and $\gamma_\perp$, respectively. Note that semi-logarithmic plot is used only for clarity.
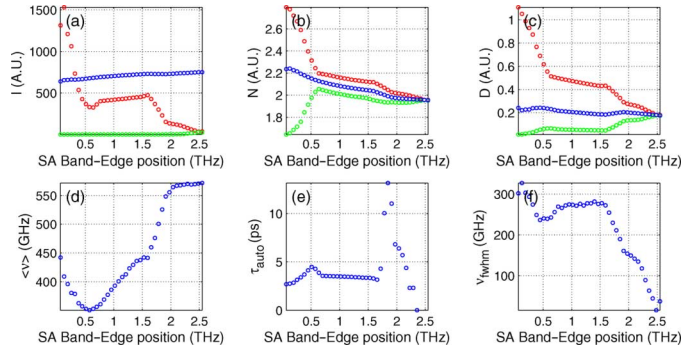

Fig. 9. Bifurcation diagram as a function of the band-edge detuning of the SA, minima, maxima and average values are depicted in green, red and blue, respectively (see text for details).

pulses by tuning the grating in order to compensate for the active material GVD. This is in full agreement with the experimental literature on semiconductor ML, see for instance the reviews in [31] and [32].

E. Influence of the Gain/Absorber Relative Frequency Shift

The former discussion indicates TGAT the detuning of the energy gaps between the gain and the absorber section is of paramount importance for generating stable ML. It was indeed pointed out in [27] that a careful tuning of the bandgap of the SA section allows for a pulsewidth reduction of more than a factor two. While the application of a reverse Voltage is an efficient way to increase the sweep out of carriers, this has also the side effect to red-shift the position of the SA band-edge frequency. For instance, typical values for the bandgap shift in Al quaternary materials are of the order of 1 THzV^{-1} [30].

As shown in Fig. 8, stable ML is only achieved for the proper spectral alignment of the gain and absorption curves. The reason is that if the SA band-edge is substantially red-detuned with respect to the amplifier, the absorption losses in the system will always be high and barely saturable; conversely, for large blue-detuning of the SA band-edge, the absorption losses are small and will always be bleached. In both cases, ML shall not occur, at

least within the framework of the quasi-equilibrium approximation. Only when the gain peak barely coincides with the SA band-edge we expect strong modulation of the absorption losses leading to stable ML.

Indeed, the bifurcation diagram in Fig. 9 indicates that stable fundamental ML is achieved only in when the band-edge of the SA lies between 0.6 and 1.6 THz. By comparing with Fig. 1 we can see that this is the region of simultaneous occurrence of high gain and relatively low, saturable absorption. The different regimes encountered are summarized as follows.

1) For Ω_s ranging between $\Omega_s = 2.5$ THz and $\Omega_s = 2.4$ THz the laser is essentially monomode.
2) For Ω_s ranging between $\Omega_s = 2.4$ THz and $\Omega_s = 2$ THz a transition to harmonic ML is found, as can be seen in Fig. 8 panel d), obtained for $\Omega_s = 2.1$ THz.
3) For Ω_s ranging between $\Omega_s = 2$ THz and $\Omega_s = 1.6$ THz the previously stable harmonic Mode Lock regime deteriorates into an unstable pulse train as can be seen in Fig. 8 panel c), obtained for $\Omega_s = 1.8$ THz.
4) For Ω_s ranging between $\Omega_s = 1.6$ THz down to $\Omega_{sa} = 0.7$ THz stable ML exists, see for instance Fig. 8 panel b), obtained for $\Omega_s = 1.3$ THz.
5) For Ω_s ranging between $\Omega_s = 0.7$ THz down to $\Omega_{sa} = 0$ the too large absorption triggers the onset of the Q-switch instability, as seen in Fig. 8 panel a), obtained for $\Omega_s = 0.6$ THz.

IV. CONCLUSION

The ML dynamics of a semiconductor Fabry–Pérot laser has been explored using a TWM complemented by a new description of the active medium polarization presented in [26]. The convolution method allows us to correctly describe in time domain the abrupt frequency dependence of the SA optical response. The effectiveness of our approach allowed us to systematically explore the influence of several important control parameters, e.g., length, recovery time and band-gap offset of the SA as well as the width of the gain curve. We have shown that for Fabry–Pérot devices, the pulse properties are to a large extent independent of the recovery time as long as it is shorter than the pulse repetition rate. We also found that, for the parameters considered, the optimal length of the SA is typically around 4%, in agreement with published experimental results. Although not directly applicable to an experiment, the study as a function of the gain bandwidth demonstrates that the main factor limiting the pulse duration is the curvature of the gain curve as well as the GVD. In addition, we thoroughly analyzed the strong dependence on the relative detuning between the gain curve and the band-edge of the SA. All the results found in our study are physically sound and in good qualitative agreement with the experimental knowledge on ML. This indicates that our modelling approach can be used, upon proper fitting of the material parameters, for optimization of the design of semiconductor ML lasers.

ACKNOWLEDGMENT

REFERENCES

[1] H. A. Haus, "Mode-locking of lasers," *IEEE J. Sel. Topics Quantum Electron.*, vol. 6, no. 6, pp. 1173–1185, Dec. 2000.

[2] E. A. Avrutin, J. H. Marsh, and E. L. Portnoi, "Monolithic and multi-GigaHertz mode-locked semiconductor lasers: Constructions, experiments, models and applications," *IEE Proc.-Optoelectron.*, vol. 147, pp. 251–278, 2000.

[3] H. A. Haus, "Theory of mode locking with a fast saturable absorber," *J. Appl. Phys.*, vol. 46, pp. 3049–3058, 1975.

[4] H. A. Haus, "Theory of mode locking with a slow saturable absorber," *IEEE J. Quantum Electron.*, vol. 11, no. 9, pp. 736–746, Sep. 1975.

[5] K. Yvind, D. Larsson, L. Christiansen, J. Mørk, J. Hvam, and J. Hanberg, "High-performance 10 GHz all-active monolithic modelocked semiconductor lasers," *Electron. Lett.*, vol. 40, no. 12, pp. 735–737, Jun. 2004.

[6] H. Dorren, D. Lenstra, Y. Liu, M. Hill, and G.-D. Khoe, "Nonlinear polarization rotation in semiconductor optical amplifiers: Theory and application to all-optical flip-flop memories," *IEEE J. Quantum Electron.*, vol. 39, no. 1, pp. 141–148, Jan. 2003.

[7] E. P. Ippen, "Principles of passive mode locking," *Appl. Phys. B*, vol. 58, pp. 159–170, 1994.

[8] J. Javaloyes, J. Mulet, and S. Balle, "Passive mode locking of lasers by crossed-polarization gain modulation," *Phys. Rev. Lett.*, vol. 97, no. 16, p. 163902, 2006.

[9] K. G. Wilcox, Z. Mihoubi, G. J. Daniell, S. Elsmere, A. Quarterman, I. Farrer, D. A. Ritchie, and A. Tropper, "Ultrafast optical stark mode-locked semiconductor laser," *Opt. Lett.*, vol. 33, no. 23, pp. 2797–2799, 2008.

[10] A. G. Vladimirov and D. Turaev, "Model for passive mode locking in semiconductor laser," *Phys. Rev. A*, vol. 72, p. 033808, 2005.

[11] G. P. Agrawal and N. A. Olsson, "Self-phase modulation and spectral broadening of optical pulses in semiconductor laser amplifiers," *IEEE J. Quantum Electron.*, vol. 25, no. 11, pp. 2297–2306, Nov. 1989.

[12] G. P. Agrawal, "Effect of gain dispersion on ultrashort pulse amplification in semiconductor laser amplifiers," *IEEE J. Quantum Electron.*, vol. 27, no. 6, pp. 1843–1849, Jun. 1991.

[13] K. Yee, "Numerical solution of initial boundary value problems involving maxwell's equations in isotropic media," *IEEE Trans. Ant. Propag.*, vol. 14, no. 3, pp. 302–307, May 1966.

[14] J. Hader, J. Moloney, and S. Koch, "Microscopic theory of gain, absorption, and refractive index in semiconductor laser materials-influence of conduction-band nonparabolicity and coulomb-induced inter-subband coupling," *IEEE J. Quantum Electron.*, vol. 35, no. 12, pp. 1878–1886, Dec. 1999.

[15] A. Vladimirov, A. S. Pimenov, and D. Rachinskii, "Numerical study of dynamical regimes in a monolithic passively mode-locked semiconductor laser," *IEEE J. Quantum Electron.*, vol. 45, no. 5, pp. 462–468, May 2009.

[16] J. A. Fleck, "Emission of pulse trains by q-switched lasers," *Phys. Rev. Lett.*, vol. 21, no. 3, pp. 131–133, Jul. 1968.

[17] M. Homar, J. Moloney, and M. San Miguel, "Travelling wave model of a multimode fabry-perot laser in free running and external cavity configurations," *IEEE J. Quantum Electron.*, vol. 32, no. 3, pp. 553–566, Mar. 1996.

[18] L. Narducci and N. B. Abraham, *Laser Physics and Laser Instabilities*. Singapore: World Scientific, 1988.

[19] H. Casey and M. Panish, *Heterostructure Lasers*. New York: Academic, 1978.

[20] C. Ning, R. Indik, and J. Moloney, "Effective bloch equations for semiconductor lasers and amplifiers," *IEEE J. Quantum Electron.*, vol. 33, no. 9, pp. 1543–1550, Sep. 1997.

[21] J. Yao, G. P. Agrawal, P. Gallion, and C. M. Bowden, "Semiconductor laser dynamics beyond the rate-equation approximation," *Opt. Commun.*, vol. 119, p. 246, 1995.

[22] S. Balle, "Effective two-level model with asymmetric gain for laser diodes," *Opt. Commun.*, vol. 119, pp. 227–235, 1995.

[23] S. Balle, "Analytical description of spectral hole-burning effects in active semiconductors," *Opt. Lett.*, vol. 21, pp. 1923–1925, 2002.

[24] S. Balle, "Simple analytical approximations for the gain and refractive index spectra in quantum well lasers," *Phys. Rev. A*, vol. 57, pp. 1304–1312, 1998.

[25] J. Javaloyes and S. Balle, "Emission directionality of semiconductor ring lasers: A traveling-wave description," *IEEE J. Quantum Electron.*, vol. 45, no. 5, pp. 431–438, May 2009.

[26] J. Javaloyes and S. Balle, "Time domain response of the semiconductor media," *Phys. Rev. A*, 2010, submitted for publication.

[27] D. Kunimatsu, S. Arahira, Y. Kato, and Y. Ogawa, "Passively mode-locked laser diodes with bandgap-wavelength detuned saturable absorbers," *IEEE Photon. Technol. Lett.*, vol. 11, no. 11, pp. 1363–1365, Nov. 1999.

[28] A. Pérez-Serrano, J. Javaloyes, and S. Balle, "Bichromatic emission and multimode dynamics in ring lasers," *Phys. Rev. A*, 2010, submitted for publication.

[29] M. Matsumoto and T. Nishimura, "Mersenne twister: A 623-dimensionally equidistributed uniform pseudo-random number generator," *ACM Trans. Model. Comput. Simul.*, vol. 8, no. 1, pp. 3–30, 1998.

[30] L. Hou, P. Stolarz, J. Javaloyes, R. Green, C. Ironside, M. Sorel, and A. Bryce, "Subpicosecond pulse generation at quasi-40-GHz using a passively mode-locked algainas-inp 1.55-μm strained quantum-well laser," *IEEE Photon. Technol. Lett.*, vol. 21, no. 23, pp. 1731–1733, Dec. 1, 2009.

[31] K. A. Williams, M. G. Thompson, and I. H. White, "Long-wavelength monolithic mode-locked diode lasers," *New J. Phys.*, vol. 6, no. 1, p. 179, 2004.

[32] R. Kaiser and B. Huttl, "Monolithic 40-GHz mode-locked MQW DBR lasers for high-speed optical communication systems," *IEEE J. Sel. Topics Quantum Electron.*, vol. 13, no. 1, pp. 125–135, Jan.–Feb. 2007.

Julien Javaloyes is with the Department of Electronics and Electrical Engineering, Glasgow, Scotland, U.K., where he focuses on the dynamics of semiconductor lasers.

Salvador Balle is with the IMEDEA, Esporles, Spain. His research focuses on the dynamics of semiconductor lasers and amplifiers.